




Remote Sensing of the Light-Obscuring Smoke Properties in Real-Scale Fires Using a Photometric Measurement Method

Kristian Börger, Computational Civil Engineering, University of Wuppertal, Wuppertal, Germany; Institute for Advanced Simulation, Forschungszentrum Jülich, Jülich, Germany

Alexander Belt, Institute for Advanced Simulation, Forschungszentrum Jülich, Jülich, Germany

Thorsten Schultze, Communication Systems (NTS), University of Duisburg-Essen, Duisburg, Germany

Lukas Arnold , Computational Civil Engineering, University of Wuppertal, Wuppertal, Germany; Institute for Advanced Simulation, Forschungszentrum Jülich, Jülich, Germany*

Received: 16 March 2023/**Accepted:** 19 July 2023/**Published online:** 22 September 2023

Abstract. A new photometric measurement method for the determination of temporally and spatially resolved light extinction coefficients in laboratory fire tests was recently presented. The approach relies on capturing the change in intensity of individual light sources (LEDs) due to fire smoke using a commercially available digital camera. Comparing the results for red light LEDs to measurements of the well-established MIREX system indicates the model is capable of capturing the investigated phenomena. However, a significant underestimation of this reference measurement taken in the infrared range is inconsistent with the expected increase of the extinction coefficients with lower wavelengths. In the context of new experimental investigations, this deficiency was remedied by evaluating multiple colour channels of RAW image data instead of the previously used JPG files. Furthermore, extending the experimental setup by several LED strips as well as a second camera allows to verify the hypothesis of a homogeneous smoke layering. The study covers eight experiments including *n*-heptane fuel in style of the well documented EN 54 TF 5 testfire as well as two additional experiments with an *n*-heptane-toluene mixture. Considering spatial resolution as well as the high reproducibility of the results, the method appears to be a convenient tool for the validation of numerical visibility models. Nevertheless, a sensitivity analysis identified uncertainties that need to be addressed in upcoming investigations to further improve the accuracy.

Keywords: Compartment fire, Visibility, Soot, Extinction coefficients, Optical measurement, Photometry

*Correspondence should be addressed to: Lukas Arnold, E-mail: arnold@uni-wuppertal.de, l.arnold@fz-juelich.de

Alexander Belt, Thorsten Schultze, and Lukas Arnold have contributed equally to this work.



1. Introduction

On the occurrence of a fire, smoke usually poses the greatest danger to the building's occupants, as it can make it difficult or even impossible to escape to a safe area. It affects both, the available safe escape time (ASET) and the time required for a safe escape (RSET). The occupants' movement speed and the capability of wayfinding are impaired by the smokes irritating products and its optical opacity. Likewise, the conditions for self-rescue become untenable when the exposure to heat or toxic smoke products exceed a critical level [1]. When modelling escape scenarios in performance-based safety designs within the ASET-RSET [2] concept, corresponding threshold values are matched against the predicted exposures. The FED (Fractional Effective Dose) model proposed by Hartzell and Emmons [3] is commonly used to assess the hazardous effects of fire induced smoke. A time-dependent incremental exposure dose is related to the total exposure dose required to cause a toxicological effect. The time at which the continuously integrated fractional effective dose for a person exceeds a certain limit indicates the time available until the person is incapable of escaping. An approach for applying both of these concepts in numerical fire simulations is outlined in [4, 5].

In contrast, modelling visibility is much more complex. It has to be considered as a spatial phenomenon rather than a local quantity. Numerical models like the Fire Dynamics Simulator (FDS) [6] rely on the concept of Jin [7], defining visibility as the distance at which a visual target can still be recognized in a smoke laden environment as the contrast to the background is sufficiently large. This approach, see Eq. 1, is highly simplified, as it merely maps visibility V as a ratio of the local extinction coefficient σ to an empirical factor C for the contrast threshold.

$$V = \frac{C}{\sigma} \quad (1)$$

Furthermore, considerable uncertainties within the modelling of visibility can arise from the experimentally obtained input parameters, that are usually encapsulated by the extinction coefficient. Gottuk et al. reported deviations by a factor of 4–5 of the optical density between large-scale experiments and simulations with FDS. They primarily attributed this to scaling effects of the soot yield, as well as soot loss due to deposition effects [8]. Similar discrepancies between experiments and corresponding simulations with FDS have been reproduced in [9].

Computational fluid dynamics (CFD) models such as FDS allow for the prediction of smoke propagation in turbulent systems on a spatial scale, which is a major advantage over zone models and hand formulas. However, spatially and temporally resolved measurements from experimental studies are in general needed to validate such complex models. In order to obtain spatially and temporally resolved extinction coefficients from the optical observation of a single LED strip within laboratory experiments, a photometric method was recently presented [10]. It relies on capturing the smoke induced attenuation of light by a digital camera. Local values of the extinction coefficient can be deduced by an inverse modelling approach based on the Beer–Lambert law and simple geometrical optics. Besides

the validation of numerical fire models, the method can contribute to the development of photometric smoke detection systems. The presented study primarily addresses the assessment of its general applicability as a photometric measurement method in laboratory test fires. In this context, the adaptability to different experimental setups, different types of fuels as well as the influence from the experimental boundary conditions are investigated. The goal of the study is to develop a reliable measurement method for the comprehensive investigation of fire smoke characteristics. A similar approach for analysing smoke density using video data from conventional security cameras is presented in [11].

The above-mentioned photometric method provides some substantial advantages, since it is easily applicable with small technical effort. Moreover, smoke propagation is not disturbed by air ducts or filters as part of a measuring apparatus. Comparison of the computed extinction coefficients within an *n*-heptane test fire in style of the EN 54 TF 5 with measurements of the well-established MIREX system shows that the method is reasonably capable of capturing the light obscuring phenomenon of the smoke. However, the observation of the results being significantly lower than the MIREX measurement does not agree with expected behaviour of the extinction coefficient increasing with decreasing wavelengths. Examining those issues is an essential part of this work.

The next section will first discuss the characteristics and properties of fire smoke, and the associated effects on light obscuration. Hereafter, the setup and procedure of the conducted experiments will be presented. An outline on the data acquisition and the methodology is provided, although it is primarily limited to the enhancements of the original approach. The subsequent section addresses the application of the method to experimental data, as well as its validation by reference measurements. Here, the focus is on investigating the temporal and spatial resolution of the computed extinction coefficients for light at different wavelengths. Finally, the uncertainties of the model and the experiments are assessed by means of a sensitivity analysis. The article closes with a conclusion and an outlook on future work.

2. Light Obscuring Effects of Fire Smoke

Investigating the effects of fire induced smoke on visibility requires an understanding of its characteristics along with the associated light obscuring properties. Mullolland provides a convenient definition of smoke as the condensed phase component of the combustion products that widely varies in appearance and structure [12]. Light-coloured aerosols, essentially containing droplets, produced by smouldering fires and pyrolysis have a strong scattering effect on light. Dark and solid carbonaceous soot particles produced by flaming combustion from fuels such as *n*-heptane, on the other hand, are highly absorbent [13]. Both effects are induced by the particle size distribution of the aerosol, mainly related to the geometric mean volume to surface diameter of the particles [14]. For post-flame smoke particles, the absorbing effect can be expressed in terms of an almost fuel type independent, mass-specific extinction coefficient, subsequently denoted K_m .

This simplification assumes that soot essentially comprises spherical carbonaceous particles significantly smaller than the wavelength of light so that scattering effects are negligible [15]. The light obscuring effect of smoke therefore is proportional to the smoke density ρ_S . Both quantities can be summarized into the extinction coefficient σ . It can be obtained by applying Beer–Lambert’s law, see Eq. 2, to optical measurements of the light transmission T along a known path length l . However, this only accounts for the damping effect on the initial light intensity I_0 to the intensity I in the presence of smoke due to absorption and scattering, since both effects can not easily be separated.

$$T = \frac{I}{I_0} = \exp(-K_m \cdot \rho_S \cdot l) = \exp(-\sigma \cdot l) \quad (2)$$

Mulholland and Croarkin estimated K_m to be $8700 \text{ m}^2 \text{ kg}^{-1}$ with an extended uncertainty of $1100 \text{ m}^2 \text{ kg}^{-1}$ as a mean value from the analysis of seven studies involving 29 fuels in flaming fires [15]. It is frequently referenced as a default quantity in various numerical fire models, such as FDS [16]. Optical measurements each were performed at a wavelength of $\lambda = 633 \text{ nm}$ in post-flame generated smoke from stoichiometric or over-ventilated combustion. For smoulder and pyrolysis generated smoke, the value is reported to be much lower and more variable. A similar study was conducted by Widmann based on a literature review of data from stoichiometric and over-ventilated combustion [17]. He deduced a correlation of K_m with wavelength λ , based on the least square fit of measurements mainly in the visible spectrum and in the near infrared range, described by Eq. 3.

$$K_m = 4.8081 \cdot \lambda^{-1.0088} \quad (3)$$

The value of K_m can change over time caused by ageing processes of the aerosol. Due to agglomeration, the particle concentration decreases while the size distribution shifts towards a larger mean particle diameter [18]. The difference in scattering and absorption characteristics of particles at different wavelengths can be used to estimate the mean particle size diameter. A potential approach relying on a combination of optical measurements and theoretical calculations based on Mie scattering theory is presented in [19, 20]. These procedures follow a correlation of the logarithms of the measured light transmission at different wavelengths with the calculated extinction efficiency as a function of the particle diameter. Węgrzyński et al. have examined several multi-wavelength densitometers following a similar approach in a literature study [21]. They summarized that most of the apparatus are connected to bench-scale experimental setups like cone calorimeters, while only few devices exist that are meant to be used in compartment scale fires. Still, such investigations are even more important in terms of modelling visibility, since scaling effects regarding the extinction coefficient can not be precluded.

3. Experimental Setup and Procedure

The presented experiments were conducted in the Heinz-Luck fire detection laboratory at the university of Duisburg-Essen, Germany. The study is based on the concept introduced in [10] and therefore features a similar design and procedure. A fundamental assumption of the model is the extinction coefficient being homogeneous within horizontal layers. To investigate this hypothesis, seven of the same type as the previously used LED strips were installed vertically (three strips) and diagonally (four strips) in the laboratory, see Figure 1. The assembly roughly spans a plane, tangent to a circle with a 3 m radius around the fire source. It extends from a height of 1 m above the floor to the ceiling at 3.37 m. Each of the strips measures an equal length of approximately 2.35 m and contains 141 RGB LEDs. The experimental setup features two DSLR cameras facing the LEDs from different locations and heights. Within two setups, the position of the second camera is varied. In setup 1, camera 1 and camera 2 are positioned on opposite sides of the room to the left and right in front of the LEDs. In setup 2, the position of camera 1 remains constant, while camera 2 is placed directly next to it, but at a slightly elevated position. Since it covers a similar distance to both cameras in setup 1, the centre LED strip serves as a reference for investigating symmetry effects. Three MIREX devices are located behind it at heights of 1.52 m, 2.3 m and 3.3 m above the floor. The MIREX apparatus measures the smoke density on a 2×1 m reflected path length according to the light transmission in the infrared regime, with a maximum intensity at a wavelength of $\lambda_{\text{IR}} = 880$ nm [22].

Data acquisition by the cameras as well as the MIREX covers a period of about 20 min and is performed at a 1 Hz sampling rate. In order to investigate the reproducibility of the experiments, all measurement sequences are evaluated

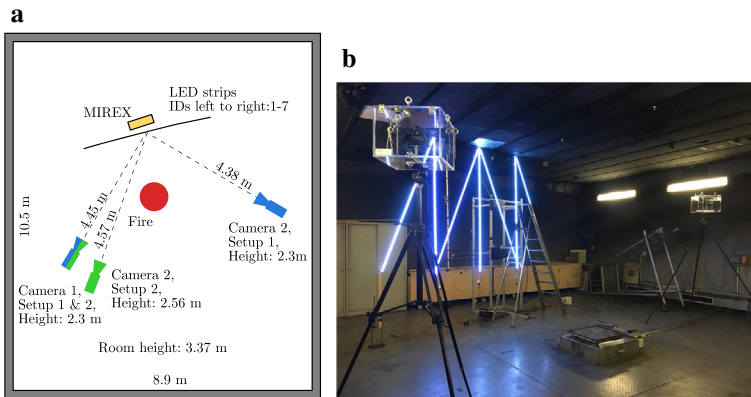


Figure 1. Experimental setup in style of EN 54. (a) Floor plan of the experimental setup. Three MIREX devices are located behind the centre LED strip. The position of the second camera varies within two setups. (b) Experimental setup before ignition of the fuel. Two cameras facing the LEDs are located left and right of the pool fire (setup 1).

starting with the time of the fuel ignition. The laboratory ventilation system is activated 6 min after that time.

3.1. Heat Release Rate

The test fires of the EN 54 standard [23] form the basis for the classification of smoke detectors and therefore should be easily reproducible. A total of eight *n*-heptane fires in style of the TF 5 test fire were investigated within the scope of the experiments. In each case, 500 g of *n*-heptane fuel were burned in a 335 mm × 335 mm fuel pan, resulting in an average burning duration of approximately 225 s. Compared to the EN 54 standard, the amount of fuel was reduced from 650 g to account for the reduced ceiling height. The mass loss rate was determined from continuous weighing so that the Heat Release Rate (HRR) could be derived from 44.6 MJ kg^{-1} for the effective heat of combustion [24]. Another series of two experiments was performed, adding 15 g of toluene to the fuel, yielding similar heat release rates.

Figure 2 shows the mass loss and the corresponding HRR as mean values from eight experiments with *n*-heptane fuel. All data were smoothed by a 5 s moving average. The narrow standard deviation confirms the good reproducibility in terms of the burning progression.

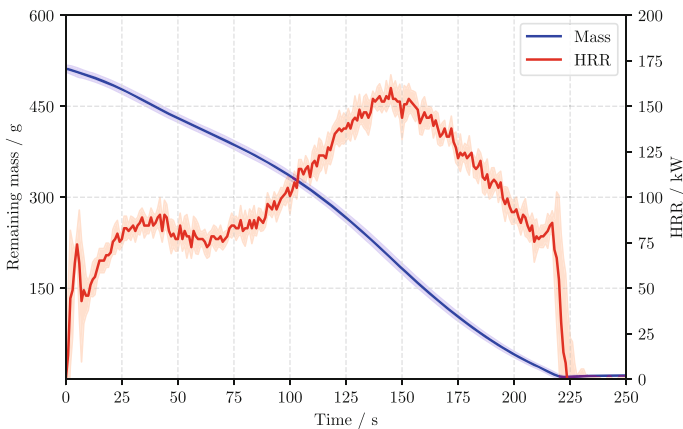


Figure 2. Mass loss and HRR for the 500 g *n*-heptane pool fires in style of the TF 5 according to EN 54. Solid lines indicate mean values, while shaded areas depict the standard deviation. The maximum HRR of approx. 159 kW is reached at about 145 s.

4. Methodology

4.1. Raw Data Acquisition

The photometric measurement method described in [10] is based on the time-resolved acquisition of LED intensities from images series. The original approach followed the procedure outlined subsequently.

Using a reference image taken before the start of the experiment, all visible LEDs are detected that exceed a certain threshold in luminosity. Iteratively, the pixel with the highest value including a peripheral area is excluded from the further search. The width of these regions of interest, further denoted ROI, is chosen to be uniform and sufficiently large. It must be ensured that the relevant pixels do not shift outside these areas due to refraction of the incident light. An image model of each LED is fitted to the experimentally obtained pixel values by means of an algebraic model. The approach allows determining the position and magnitude of the amplitude from the shape of the modelled LED. Acquiring these quantities potentially allows for the consideration of extensive phenomena, such as refraction. However, since this process has to be repeated for all images and LEDs, it requires an enormous computational effort.

As the focus of the current study is on the acquisition of significant amounts of data, a simplified approach to determine the LED intensities is used for that purpose. At each time step, the LED intensity is calculated separately for all three colour channels (CH) as the sum of all pixel values within the respective ROI.

The camera exposure is primarily determined by shutter speed, aperture, and the sensor sensitivity (ISO). For photometric measurement, it therefore is essential to operate the camera in manual mode (see Table 1) and to deactivate any internal image optimization.

Nevertheless, luminosity measurements based on JPG images is inevitably biased by camera-internal preprocessing. For example, a correction function (e.g., gamma correction) is usually applied to scale linear sensor data according to the logarithmic light sensitivity of human perception. However, high-quality CCD or CMOS cameras do allow direct access to the unprocessed sensor data via RAW image files.

The camera sensor is covered with a spectrally sensitive colour filter array (CFA) arranged according to a particular mosaic pattern, of which each element only samples a single colour. The resulting intermediate greyscale image can be converted to a true-colour image by various interpolation techniques referred to as ‘demosaicing’, in which each pixel typically maps independent levels for red (R), green (G), and blue (B) [25]. The most common CFA is the Bayer filter

Table 1
Manual Settings of the Used Cameras

Camera	Model	ISO	Shutter speed	Aperture	Focal length
1	Canon 80D	100	1/500 s	f/16	18 mm
2	Canon 70D	100	1/250 s	f/22	18 mm

array, which is also used in the employed cameras. A regularly repeating 4×4 pixel section of this pattern is shown in Figure 3. Like most CFAs, it contains twice as many green-sensitive filters, which is supposed to match human perception in terms of higher resolution for green light.

4.2. Determining the LED Intensities

Since the unprocessed RAW images are encoded in a native camera file format, the embedded data is accessed by a Python wrapper for the LibRaw library [26]. The obtained sensor readings can be represented as a matrix $S(x, y)$ of elements with positions x, y , that has the same resolution as the visible part of the sensor. In order to convert this matrix into a greyscale image with pixels $P(x, y)$, the individual elements must be mapped to a fixed tonal range [27] by Eq. 4.

$$P(x, y) = (S(x, y) - B) \cdot \frac{2^{b-1}}{W - B} \quad (4)$$

B and W indicate the black level and the saturation point of the sensor. The black level is measured using masked pixels, i.e., pixels which are not illuminated by construction, and thus serves as a calibration point for the sensor noise, e.g., due to temperature influences. After linearizing the sensor readings within those bounds, they are scaled back to integer values according to the target tonal range b . JPG images usually feature a tonal range of 8 bit, allowing each colour channel to be shaded in 256 increments. The sensor data, on the other hand, are typically recorded at a 14-bit resolution. However, the higher dynamic range of RAW images is also relevant for accurate brightness measurement. It prevents details in regions with particularly high or low exposure from being irreversibly clipped by the camera's post-processing.

According to their position in the CFA, the three colour channels (RGB) can be separated as independent pixel arrays:

G _{0,0}	R _{1,0}	...	R _{x,0}
B _{0,1}	G _{1,1}	...	R _{x,1}
...	R _{x,2}
B _{0,y}	G _{1,y}	B _{2,y}	G _{x,y}

Figure 3. Bayer filter array is the most common CFA used in modern digital cameras. Red (R), green (G) and blue (B) filters are placed on the sensor by a 4×4 repeating pattern (Color figure online).

$$\begin{aligned}
 P_R(x,y) &= \begin{cases} P(x,y) & \text{if } x \text{ is odd and } y \text{ is even} \\ 0 & \text{otherwise} \end{cases} \\
 P_G(x,y) &= \begin{cases} P(x,y) & \text{(if } x \text{ is odd and } y \text{ is odd) or (if } x \text{ is even and } y \text{ is even)} \\ 0 & \text{otherwise} \end{cases} \\
 P_B(x,y) &= \begin{cases} P(x,y) & \text{if } x \text{ is even and } y \text{ is odd} \\ 0 & \text{otherwise} \end{cases}
 \end{aligned} \tag{5}$$

Figure 4 shows an example of the pixel values within the ROI of a single LED, separated for the three colour channels of the camera.

For the individual colour channels, the experimental intensity I_e simply results as the sum of the pixel values within the respective ROIs, see Eq. 6, normalized to their initial values.

$$I_e = \sum_{\text{all pixels } x,y} P(x,y) \tag{6}$$

The initial intensity I_0 of each LED indicates the mean value from 10 images taken before the fuel is ignited. It is assumed to be constant throughout the experiment and therefore serves as a reference according to Eq. 2. The influence of the variability of I_0 due to intrinsic as well as extrinsic influences by, e.g., temperature on the computation of extinction coefficients is discussed in Sect. 5.2.

Splitting the greyscale image into the individual colour channels implies that, unlike the JPG image, much fewer pixels are involved in determining the LED intensities. This can slightly increase noise. Especially within the blue and red colour channel, individual peaks of luminosity may not be detected due to a refraction induced shift of the incident light.

An instantaneous comparison of the measured intensities from a single RAW image and the corresponding JPG is given in Figure 5. It depicts the intensities for all LEDs of the centre strip about 300 s after the ignition, scaled to their initial

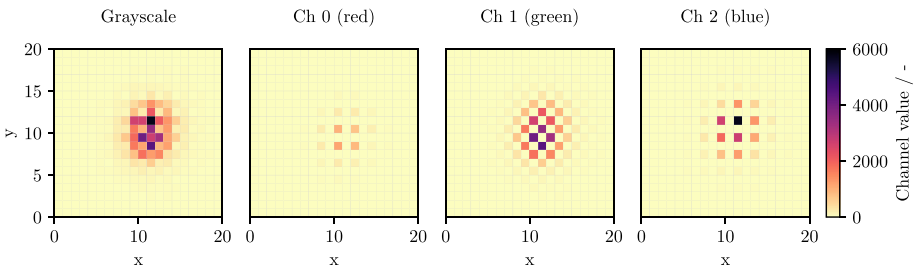


Figure 4. ROI of a greyscale image and RGB components according to the Bayer filter pattern (Color figure online).

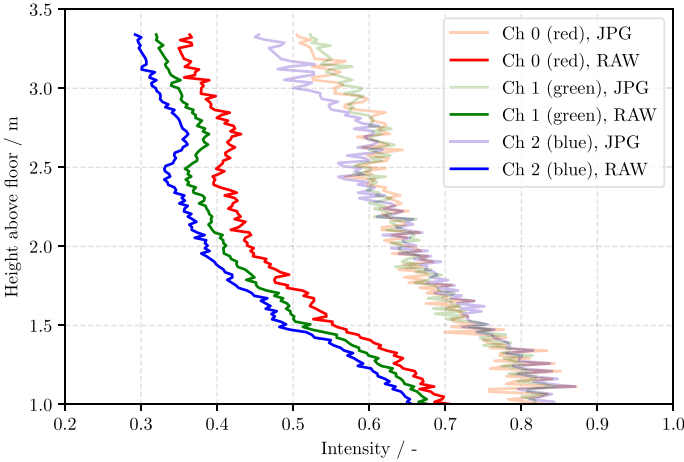


Figure 5. Normalized intensities of all 141 LEDs from the centre strip, acquired from RAW and JPG image data at $t = 300$ s. The relative deviation in the drop of intensities increases towards the lower regions.

value. The intensities from the RAW data show considerably higher attenuation than those from the corresponding JPGs, with the relative deviation in the drop of intensities increasing towards lower regions. This results in a significant underestimation of the computed extinction coefficients based on JPG images. It also entails that the wavelength influence on light obscuration can be detected exclusively in high smoke density regions. The main reason for these errors is likely to be the nonlinear scaling of the pixel values by the gamma correction.

Unlike the original approach, the experiments presented in this study are entirely analysed on the basis of RAW image files.

4.3. Computation of Extinction Coefficients

The conducted experiments are analysed by an enhanced version of the method introduced in [10]. The software LEDSA (LED Smoke Analysis) used for data analysis is written in Python [28]. An inverse modelling approach based on geometrical optics and the Beer–Lambert law is applied to obtain temporally and spatially resolved extinction coefficients σ . Therefore, a model for the intensities of individual LEDs is formulated as a line of sight integral corresponding to a spatial discretization as horizontal layers. The underlying assumption of the model is that σ is homogeneous within horizontal layers. A non-linear system of equations comprising the model intensities $I_{m,j}$ and the experimental intensities $I_{e,j}$ for all LEDs then is to be solved to find the best matching set of the extinction coefficients for each time step. $I_{e,j}$ corresponds to the accumulated pixel values according to Eq. 6 as a mean value of two consecutive images. The computation is performed separately for the three colour channels of the camera, as well as the seven LED strips.

By means of a cost function Ω_σ , see Eq. 7, additional boundary conditions besides the L2-norm between $I_{e,j}$ and $I_{m,j}$ can be considered.

$$\Omega_\sigma = \sum_{j=1}^{N_{\text{LEDs}}} (I_{m,j} - I_{e,j})^2 + \phi_s \sum_{i=2}^{N_{\text{layers}}-1} (\sigma_{i-1} - 2\sigma_i + \sigma_{i+1}) + \phi_a \sum_{i=1}^{N_{\text{layers}}} \sigma_i \quad (7)$$

The factor ϕ_s weights the requirement of a smoothness of the solution as a numerical approximation of the second derivative. Furthermore, an upper or lower limit can be defined via ϕ_a , so that either large or small values for the extinction coefficient are preferred when there is little impact of the L2-norm. This is crucial in the boundary layers, which are only crossed by few light beams. Here the information used in the optimization procedure is sparse, which leads to a weak solution, i.e., a not unique solution. By using the weighting factors, ϕ_a the solution is stressed towards bounding limits of possible values. In layers which are crossed by many light beams the solution is rigid, thus a stressing by the ϕ_a leads to same solutions. Figure 6 depicts the impact of featuring high or low values and no preference for the extinction coefficient using data from the centre LED strip. As the whole study, the analysis is based on a model with 20 equally sized layers extending from 0.99 m above the floor to the ceiling at 3.37 m height.

The extinction coefficients obtained at different wavelengths may finally serve for the remote estimation of the mean particle size. Techniques as described in [14, 19] rely on the log ratios of extinction coefficients and therefore are highly sensitive to uncertainties, e.g., from numerical artefacts. The major impact of ϕ_a as well as the significant differences among the individual colour channels in the top layers indicate that the obtained data may not be used unrestricted for this purpose.

5. Results

5.1. Extinction Coefficients

Eight experiments were performed with *n*-heptane fuel and two more with an *n*-heptane toluene mixture. The location of the second camera was varied among the experiments according to Figure 1. Therefore, the following experiments, given an identical setup, were aggregated within the evaluation:

1. Four experiments with *n*-heptane fuel in setup 1
2. Four experiments with *n*-heptane fuel in setup 2
3. Two experiments with *n*-heptane toluene mixture in setup 2

Figure 7 shows the extinction coefficients for the centre LED strip based on the photometric measurements from both cameras in setup 1. The results for layers 0, 8 and 15 correspond to the respective heights above the floor at which the reference measurements were acquired by the MIREX devices (3.30 m, 2.30 m, 1.52 m).

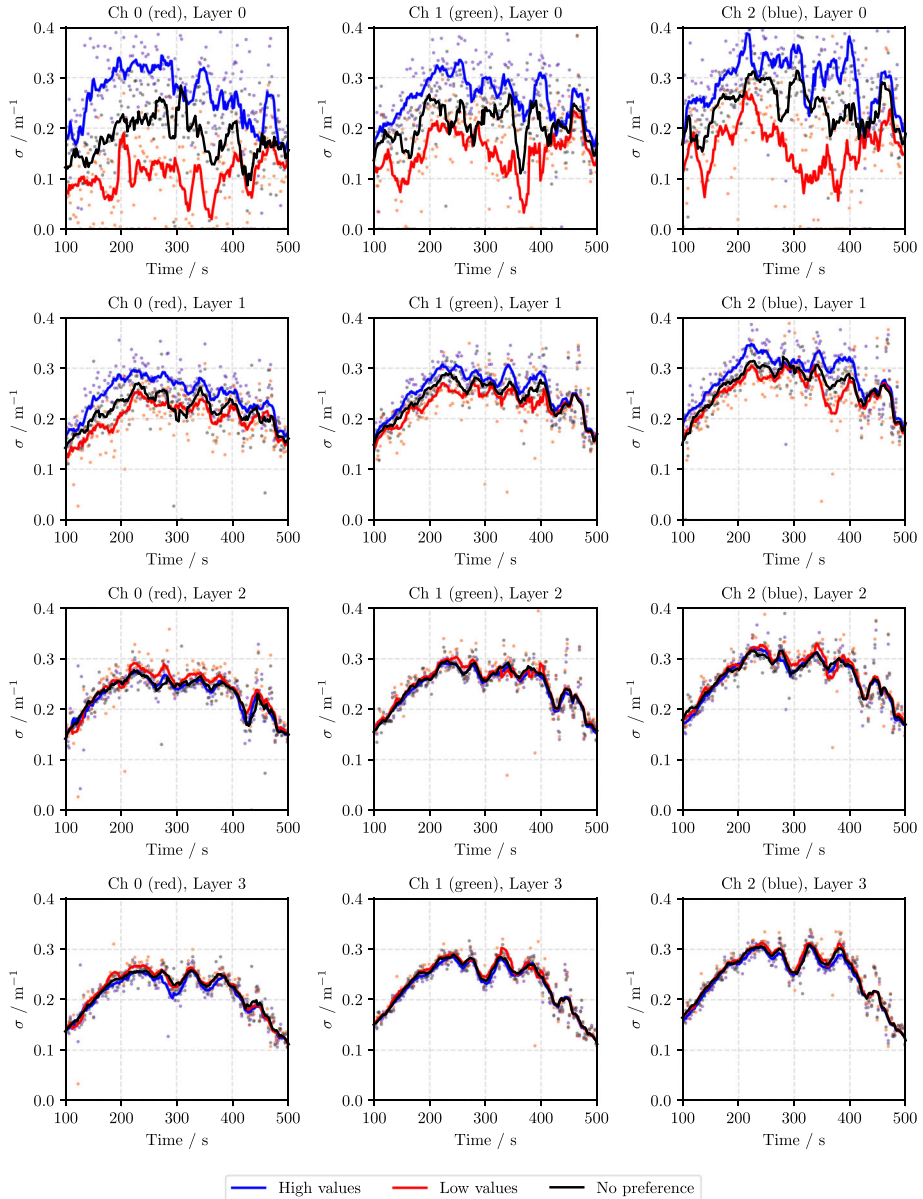


Figure 6. Influence of the weighting factor ϕ on the temporal evolution of the extinction coefficient for the three colour channels on the layers 0 to 3 (from top down). The investigation was carried out for $\phi_a = -1 \times 10^{-6}$ (low values), $\phi_a = 1 \times 10^{-6}$ (high values) and $\phi_a = 0$ (no preference). Scattered dots show the computed extinction coefficients based on the average intensities of two consecutive images each. Lines represent the smoothed data by a 10 s moving average over 5 time steps each.

The LEDSA results as well as the MIREX reference measurements confirm a good reproducibility of the experiments, which has already been shown for the mass loss. Results from both cameras are in the same order of magnitude. As expected, the extinction coefficients from LEDSA are much higher than those from the MIREX, which can be attributed to the difference in wavelengths. A strong wavelength dependence is also evident in the colour channels of the cameras. The phenomenon of increasing light obscuration with decreasing wavelength, as described by Widmann, can be observed for all data sets. According to Eq. 3, a rough estimate of the expected ratio of extinction coefficients can be established based on the peak wavelengths of the LEDs. Referring to the red LED at $\lambda_R = 630\text{ nm}$, the expected ratios are 1.24 for the green ($\lambda_G = 510\text{ nm}$), 1.37 for the blue LEDs ($\lambda_B = 462\text{ nm}$) and 0.71 for the MIREX ($\lambda_{\text{IR}} = 880\text{ nm}$), which is a good approximation especially for the eighth layer. It must be noted, however, that the light sources used are not perfectly monochromatic and the LEDs in particular have a relatively broad spectrum, which may bias this correlation. In layer 0, there is a significantly smaller discrepancy between LEDSA and the MIREX, although a distinct wavelength dependency remains evident. Potential reasons for this may be attributed to, e.g., different particle sizes of the smoke or an inhomogeneous smoke layering that effects the LEDSA layer model. However, the exact causes for this are not yet understood and will be the subject of future research.

Figure 8 shows the extinction coefficients for another series of four experiments on the setup 2. The experimental boundary conditions as well as the analysis match the one from the first setup, except that both cameras were placed side by side with a difference in height of 25 cm.

Both cameras show similar results to the first setup, but still match closer, especially in the range between 200 s and 400 s. This suggests that the discrepancies are related to the viewing angle as well as local variations in smoke density rather than intrinsic camera characteristics.

In setup 2, an additional series of two experiments was performed with toluene added to the *n*-heptane fuel (see Figure 9). The computed extinction coefficients as well as the MIREX measurements are significantly higher than for the pure *n*-heptane fire. Although the recorded dynamics of both methods match well again, it can be seen that the wavelength related ratio is not consistent with Eq. 3. The computed extinction coefficients for the red channel are of the same order of magnitude as the corresponding MIREX 1 and MIREX 2 measurements after about 300 s. A possible contribution to this may be related to a much larger mean particle diameters reported for smoke of toluene fires [29]. Jin concluded from his experiments that the dependence on wavelength vanishes or reverses for particles larger than $1\ \mu\text{m}$ [30]. However, this effect was not further investigated in this study.

Figure 10 depicts the layer wise extinction coefficients for both of the outer and the centre LED strip at 300 s as a 10 s average. For reference, the extinction coefficients were computed considering all the 987 LEDs in the setup, referred to as 'merged strips' in the plot. The minimization procedure requires the weighting of

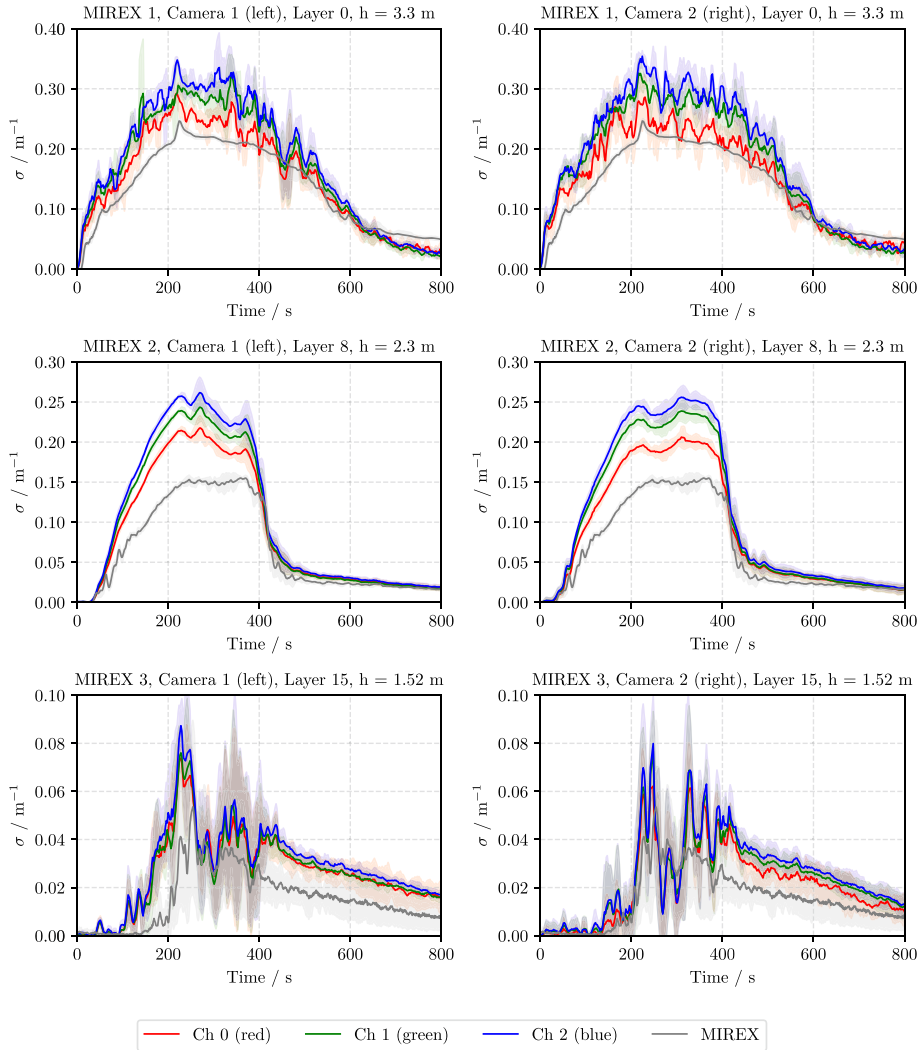


Figure 7. MIREX and LEDSA (Camera 1 and Camera 2) extinction coefficients in setup 1. The plot shows mean values (solid lines) and standard deviation (shaded areas) from four experiments with the n -heptane fuel.

the smoothness condition to be reduced via $\phi_s = 1 \times 10^{-7}$ in order to compute reasonable results.

The extinction coefficients of all LED strips follow a similar profile over the height. Especially, the results from the centre strip are in a good agreement with those from the merged strips. It should be noted that the extinction coefficients each increase with shorter distance between the reference point and the camera.

The effect is significantly larger for the red than for the green and blue camera channel.

The phenomenon also occurs in reverse for the second camera, as can be seen from the aggregated results of all strips in Figure 11. This cannot be attributed exclusively to an inhomogeneity of the smoke layering, since the influence on all colour channels would be equivalent. A change in particle size distribution could have a different effect on light opacity at various wavelengths, but this cannot be accounted for the dependence on the distance between the camera and the light source.

The observations suggest that the photometric measurement could be biased by a change in the initial luminosity of the individual light sources. A potential temperature-related effect on the emitted intensity is discussed in the following section.

Plots of the spatially resolved extinction coefficients corresponding to Figure 11 are provided in appendix A for the other colour channels.

5.2. A Study on Experimental Parameters

The Beer–Lambert law imposes some limitations that involve certain simplifications and inaccuracies for the present model. No distinction is made between effects from absorption and scattering by smoke particles, since it only describes the attenuation of a single light beam. This approach can be considered sufficiently accurate for point light sources as long as the absorbing influence is dominant over the scattering effect. For most smoke products, this assumption is valid, as the particle diameter is usually well below the wavelength of the light [15].

Another simplification of the applied method results from how the interaction between the light source and the detector is processed. For simplicity, the employed RGB LEDs are considered as three independent light sources each, which are detected solely in the respective colour channels of the camera. Since a real light source is not perfectly monochromatic and σ is a function of the wavelength, the total transmission T would be obtained by integration over its spectral bandwidth [31]:

$$T = \frac{I}{I_0} = \frac{\int_{\lambda_1}^{\lambda_2} I_0(\lambda)e^{-\sigma l} d\lambda}{\int_{\lambda_1}^{\lambda_2} I_0(\lambda)d\lambda} \tag{8}$$

Furthermore, it is assumed that the sensor’s colour filters have a perfectly flat spectral response. The related error is difficult to quantify as it results from various influences:

1. Due to the broad response spectra of the colour filters, contributions from all three colour components of the LEDs are detected in all colour channels of the camera.

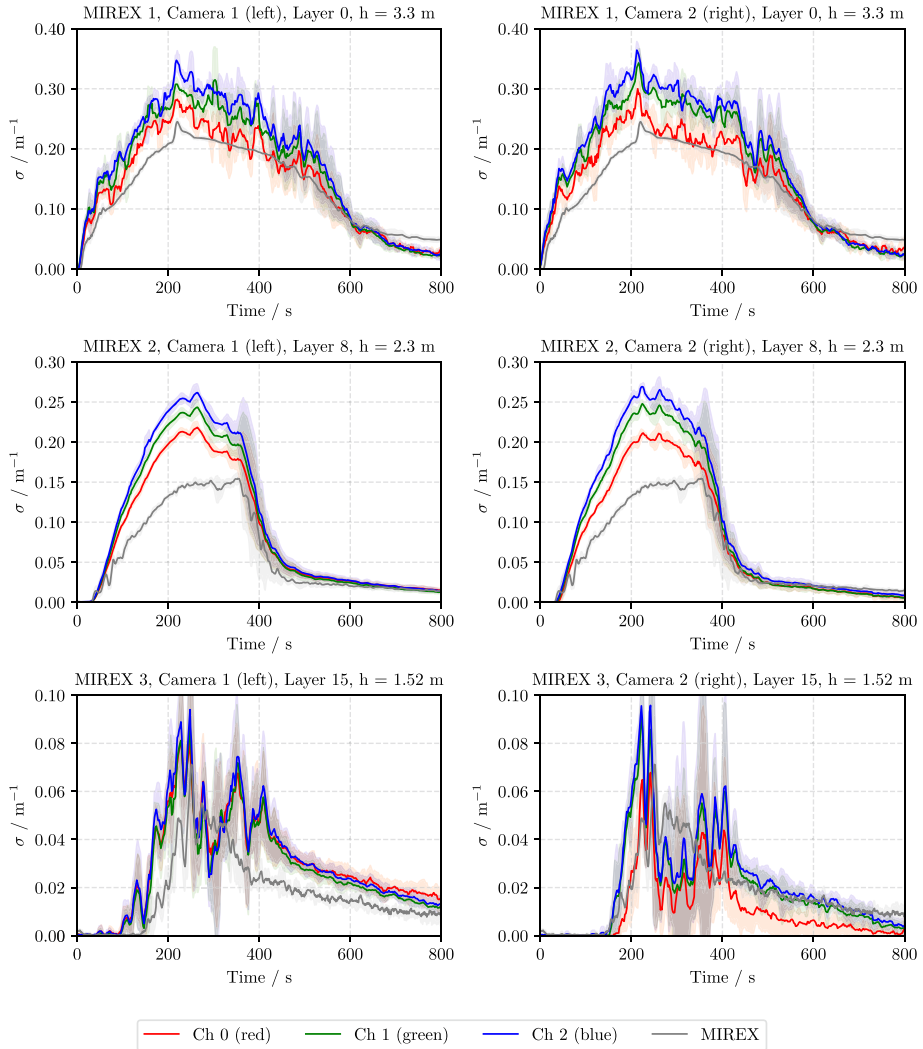


Figure 8. MIREX and LEDSA (Camera 1 and Camera 2) extinction coefficients in setup 2. The plot shows mean values (solid lines) and standard deviation (shaded areas) from four experiments with the *n*-heptane fuel.

2. Temperature-related influences may cause the emitted spectrum to vary in intensity as well as in bandwidth and peak wavelength.
3. The light attenuation caused by smoke depends on the wavelength.

The response spectrum as well as the sensitivity of the camera can be assumed to be invariable, since they are shielded from thermal exposure.

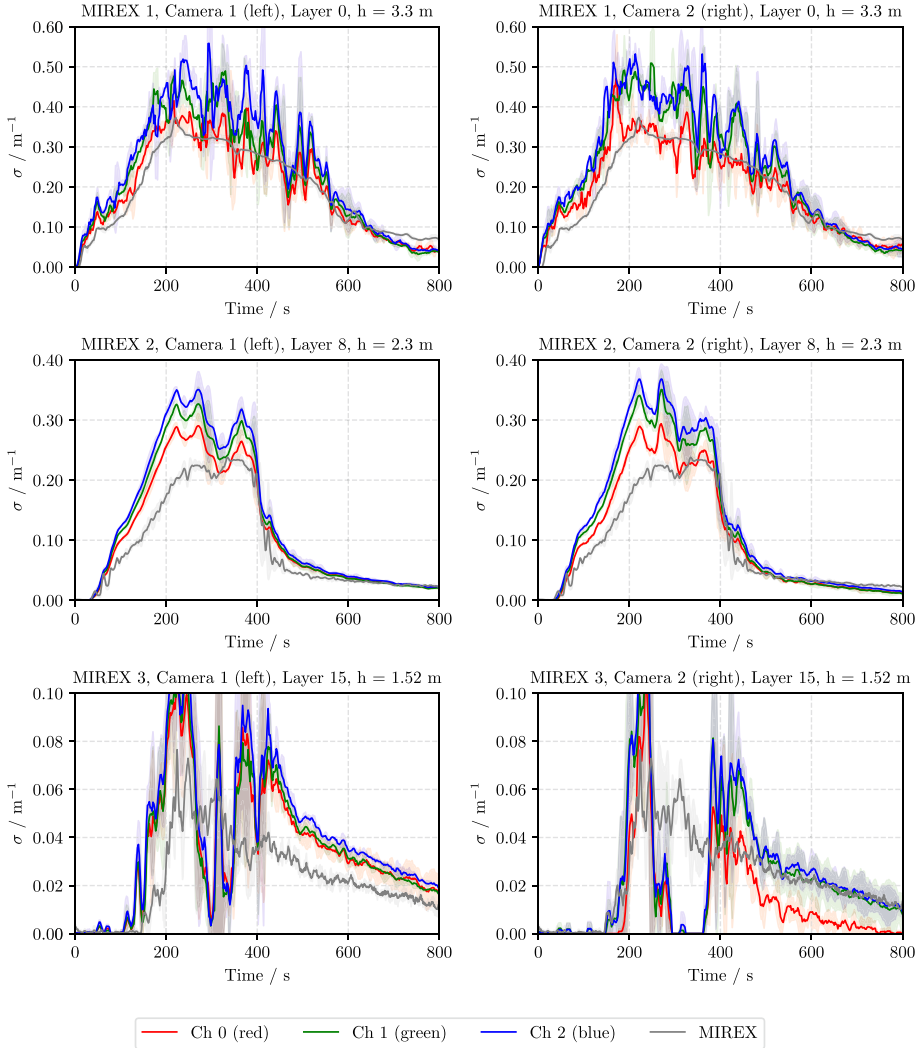


Figure 9. MIREX and LEDSA (Camera 1 and Camera 2) extinction coefficients in setup 2. The plot shows mean values (solid lines) and standard deviation (shaded areas) from two experiments with a mixed fuel from *n*-heptane and toluene.

To better understand the above influences, the LEDs used in the experiment were spectrally analysed. Figure 12 shows an example of the mean emitted spectrum of eleven RGB LEDs from three repetitive measurements with a BTS256-LED spectroradiometer device from Gigahertz-Optik [32]. All measurements were performed at ambient temperature after a ten-minute warm-up period with all three colour components turned on.

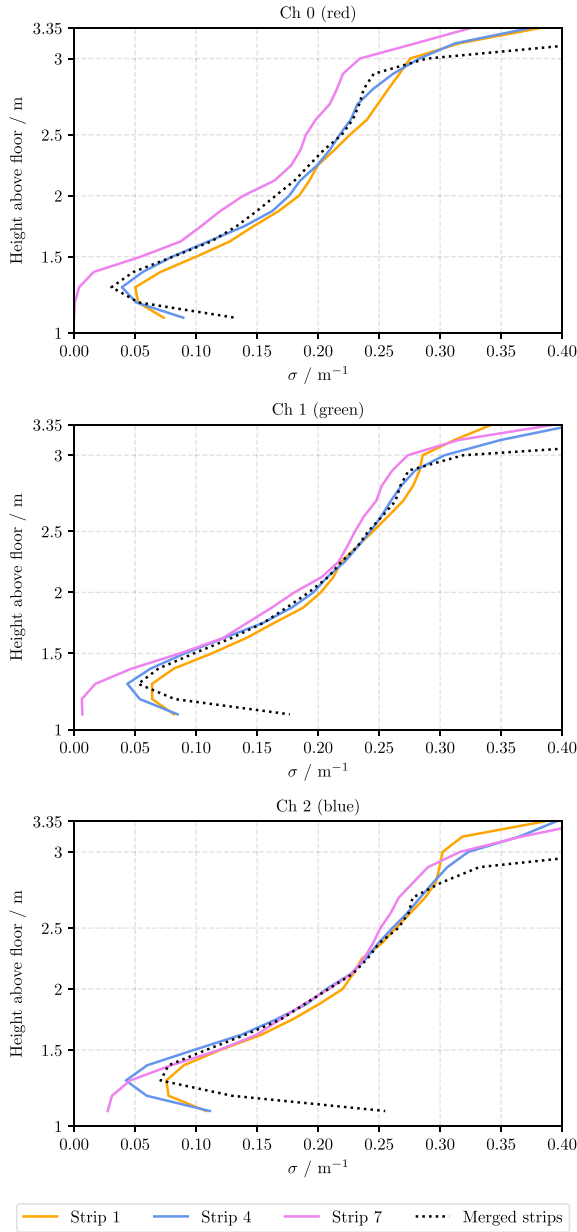


Figure 10. Computed extinction coefficients at $t = 300$ s of a single experiment for camera 1 as a function of height. The results of all three colour channels are shown for the two outer (1, 7) and the middle (4) LED strip as well as a merged computation from all strips.

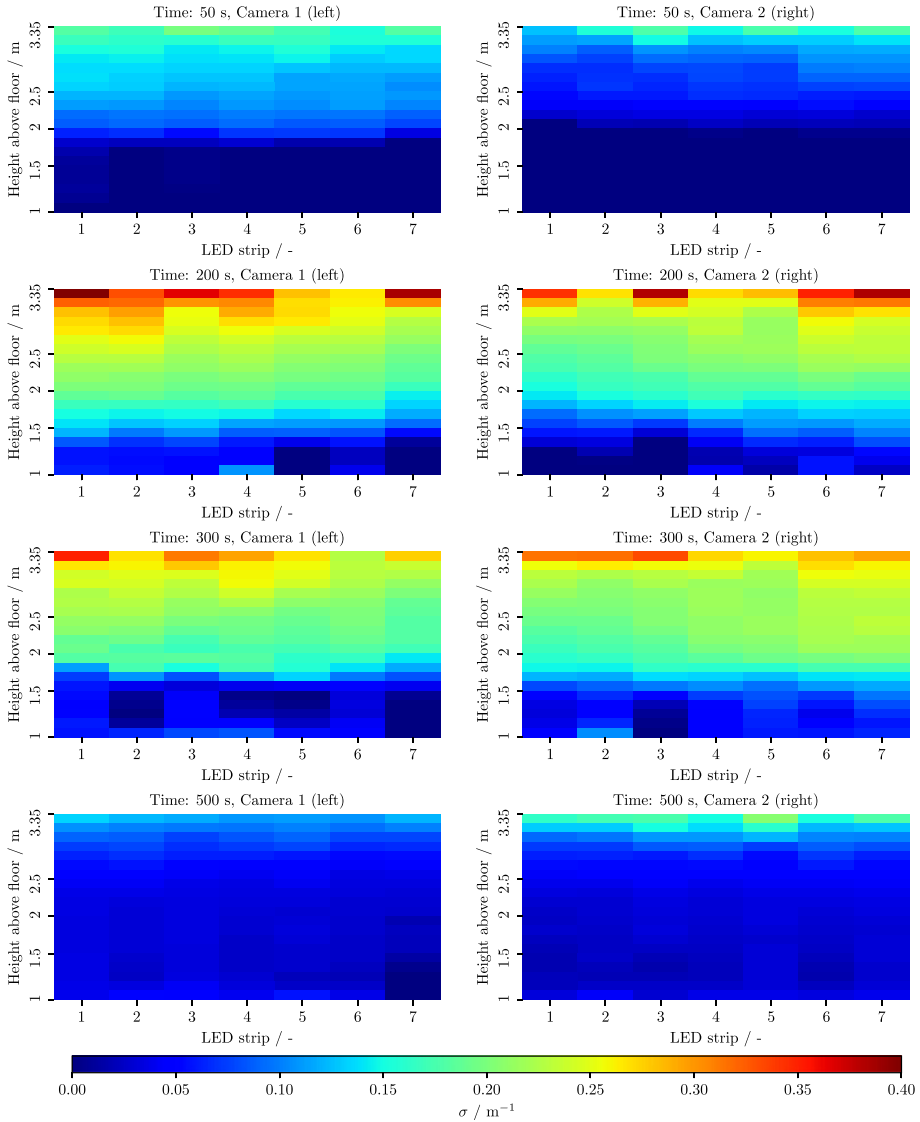


Figure 11. 2D spatial resolution of the computed extinction coefficients for the red camera channel (Channel 0) at different times for both cameras. The computed values from both cameras show a roughly point-symmetric behaviour around the centre LED strip. This phenomenon can be attributed to temperature-related influences on the LEDs as well as to a slightly homogeneous smoke layering (Color figure online).

The standard deviation of the peak wavelength is relatively small, although significantly larger for the red (1.36 nm) and blue (1.37 nm) than for the green (0.37 nm) LEDs. The coefficient of variation (CV) denotes the relative standard deviation and thus serves as a reference value that is independent of the absolute intensity. It is likewise higher for red (CV = 11.6%) and blue (CV = 15.9%) than for green (CV = 3.5%) LEDs. The RGB light sources of the individual LEDs were each analysed simultaneously, so that uncertainties in the measurements can be excluded from being a potential cause for the magnitude of deviations. Since the LED intensities are scaled to towards their initial values in the experiments, those deviations do not pose a fundamental issue for the photometric measurement. However, an uncertainty arises from the captured light in a colour channel of the camera being composed of varying contributions from the LED colour components.

Thermal exposure of the LEDs due to convective heat transfer and radiation from the plume could pose a significant error on the measured intensities. An empirical correlation between ambient temperature T and the relative emission intensity I for red AlGaInP/GaAs, green GaInN/GaN and blue GaInN/GaN LEDs from data of the Toyoda Gosei Corporation is reported in [33]:

$$I = I_{300\text{K}} \cdot \exp\left(-\frac{T - 300\text{K}}{T_1}\right) \quad (9)$$

$I_{300\text{K}}$ is the initial intensity at room temperature, here 300 K, and T_1 is the characteristic temperature. The latter is an empirical quantity characterizing the temperature dependence of the LED. Reported characteristic temperatures of $T_1 = 199\text{K}$ for red ($\lambda_{\text{R}} = 625\text{nm}$), $T_1 = 341\text{K}$ for green ($\lambda_{\text{G}} = 525\text{nm}$) and $T_1 = 1600\text{K}$ for blue ($\lambda_{\text{B}} = 460\text{nm}$) LEDs imply a much higher temperature dependence for red than for green and blue LEDs. The exact specifications of the LEDs used in the presented experiments are not known. However, it can be assumed that these are the same types as in the reported study, since they are the most commonly used today.

Temperature measurements taken close to the ceiling during the experiments allow a rough estimate of the influence on the emitted intensity based on these correlations. Maximum temperatures between 60°C and 75°C would estimate attenuation against room temperature according to Eq. 9 as follows:

- Red: 85%–79%
- Green: 91%–87%
- Blue: 98%–97%

The actual error with respect to the measurement of light transmission is likely to be smaller due to the inherent heating of the LEDs themselves, which sets in even before the external temperature exposure.

Based on this thermally induced reduction of the initial intensity I_0 , a geometric influence on the measurement of the extinction coefficient occurs. Beer–Lambert’s law assumes I_0 of the emitted light to remain constant over the entire course of the experiment. A shift of this reference thus also has an effect on the extinction coefficients computed by LEDSA. The initial intensity I_0 of an LED may be

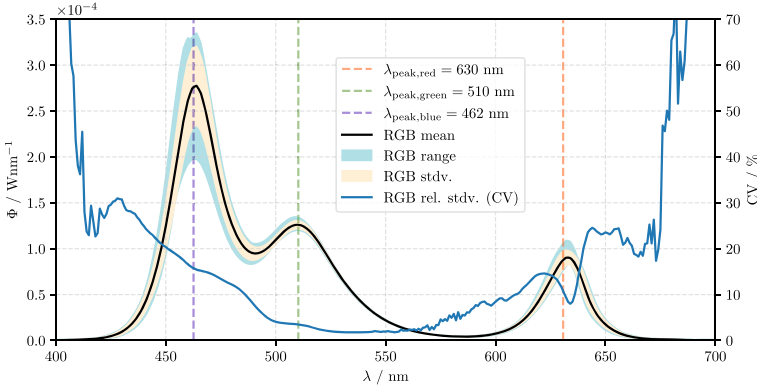


Figure 12. Mean emitted spectra of 11 RGB LEDs at ambient temperature from three repetitive measurements after a 10 min warm-up period. Furthermore, the measurement range and the standard deviation are shown. The blue line indicates the relative standard deviation (coefficient of variation (CV)) of the measured LED intensity (Color figure online).

reduced to a fraction α due to thermal exposure. Following Eq. 2 the measured intensity I_α can be expressed as a function of α and l :

$$I_\alpha = \exp(-\sigma_r \cdot l) \cdot I_0 \cdot \alpha \quad (10)$$

Here σ_r denotes the 'real' extinction coefficient that would result from a measurement with an undisturbed reference quantity I_0 . Substituting Eq. 10 into Eq. 2 and solving for σ provides the distorted extinction coefficient computed by the model, subsequently referred to as σ_m , see Eq. 11. In case $\alpha < 1$, σ_m increases against the real value σ_r with decreasing path length l through the smoke layer.

$$\sigma_m = \sigma_r - \frac{\ln \alpha}{l} \quad (11)$$

Equation 11 potentially allows determining the attenuation α of the initial intensity using the extinction coefficient calculated with LEDSA at different path lengths. However, this would require σ_r to be perfectly uniform along both measurement paths.

6. Conclusions

Experiments in style of EN 54 were conducted in order to investigate the light obscuring effects of fire smoke using a photometric method. This involves capturing the light attenuation of individual RGB LEDs on seven strips by two cameras from different perspectives. Comparing the results with local measurements of the well-established MIREX system reveals that the method is capable of computing spa-

tially and temporally resolved extinction coefficients. The LEDSA extinction coefficient values show higher fluctuations than the MIREX, which may be related to a longer measurement distance as well as the numerical optimisation procedure. However, there is no information about an internal smoothing of the raw data by the MIREX. Due to the different wavelengths of the light sources, the LEDSA extinction coefficient values are generally higher than the MIREX values at the respective measurement locations. For the MIREX at heights 1.52 m and 2.3 m, the discrepancies approximately correspond to the expected ratio according to Widmann's empirical law. For the MIREX at 3.3 m, the results of LEDSA and the MIREX are closer than expected, given the different wavelengths. A reasonable reproducibility can be verified by data from 10 experiments with *n*-heptane fuel and a mixture of *n*-heptane and toluene. Furthermore, the experimental setup allows verifying the hypothesis of homogeneous smoke properties within horizontal layers.

Significant improvements of the previously introduced photometric approach could be achieved in particular by evaluating RAW image data instead of common JPG files. The luminosity can thus be determined separately for three colour channels of a common digital camera without being corrupted by camera-internal postprocessing. However, a sensitivity analysis involving experimental data indicates that the measurement may still be biased due to a considerable temperature dependence of the LEDs.

The experimental uncertainties, especially with respect to the intrinsic properties of the LEDs, are still too large at the present stage to derive further conclusions about smoke properties such as particle size. Nevertheless, the method can be considered as a promising approach for the validation of numerical fire simulation models due to the temporal and spatial resolution. Simulations with FDS have already shown that the method is able to roughly capture the local dynamics of the smoke density. However, the results still show significant deviation, indicating the choice of unsuitable input quantities, e.g., the mass-specific extinction coefficient or the soot yield for the simulation model.

The software LEDSA which is used for data analysis was written in Python and is made freely available by the authors [28]. Additionally, all data associated with the presented experiments are publicly accessible in a Zenodo repository [34]. This involves both image files and input files comprising the geometric parameters of the setup and the boundary conditions of the model.

7. Outlook

As stated above, the applied method can be generally validated within the scope of the conducted experiments. Nevertheless, both the experimental setup and the data analysis reveal a considerable potential for improvement. To enhance the accuracy of the photometric measurement, it is essential to minimize the temperature related influences on the light sources. Higher quality LED strips with thermal insulation may therefore be used in upcoming experiments. It has been found that the latter usually also show smaller deviations in the spectrum of the individual colour sources.

The experimental setup is to be extended by further measuring devices for local detection of temperatures, light transmission and particle size distribution in order to validate the spatial resolution of the model.

Along with the data analysis from several LED strips, the employed layer model is capable to confirm the assumption of an adequate homogeneous smoke stratification. Nevertheless, it can be expected that by extending the model to a true three-dimensional scale, based on data from multiple cameras and viewpoints, local variations in smoke density can be detected. The development of such a model will include the use of synthetic measurement data from CFD simulations.

The results from the experiments with an *n*-heptane toluene mixture indicate that the fuel-specific properties affecting the particle size distribution have a measurable influence, being accounted for by this approach. Further experiments will be conducted to investigate such effects, taking into account additional test fires in accordance with EN 54, including smouldering fires and pyrolysis.

Acknowledgements

The authors gratefully acknowledge the financial support of the German Federal Ministry of Education and Research. The extensive LEDSA computations were performed largely on the high-performance computer system funded as part of the CoBra project with the Grant Number 13N15497.

Funding

Open Access funding enabled and organized by Projekt DEAL.

Open Access This article is licensed under a Creative Commons Attribution 4.0 International License, which permits use, sharing, adaptation, distribution and reproduction in any medium or format, as long as you give appropriate credit to the original author(s) and the source, provide a link to the Creative Commons licence, and indicate if changes were made. The images or other third party material in this article are included in the article's Creative Commons licence, unless indicated otherwise in a credit line to the material. If material is not included in the article's Creative Commons licence and your intended use is not permitted by statutory regulation or exceeds the permitted use, you will need to obtain permission directly from the copyright holder. To view a copy of this licence, visit <http://creativecommons.org/licenses/by/4.0/>.

Appendix: A Spatiotemporal Extinction Coefficients

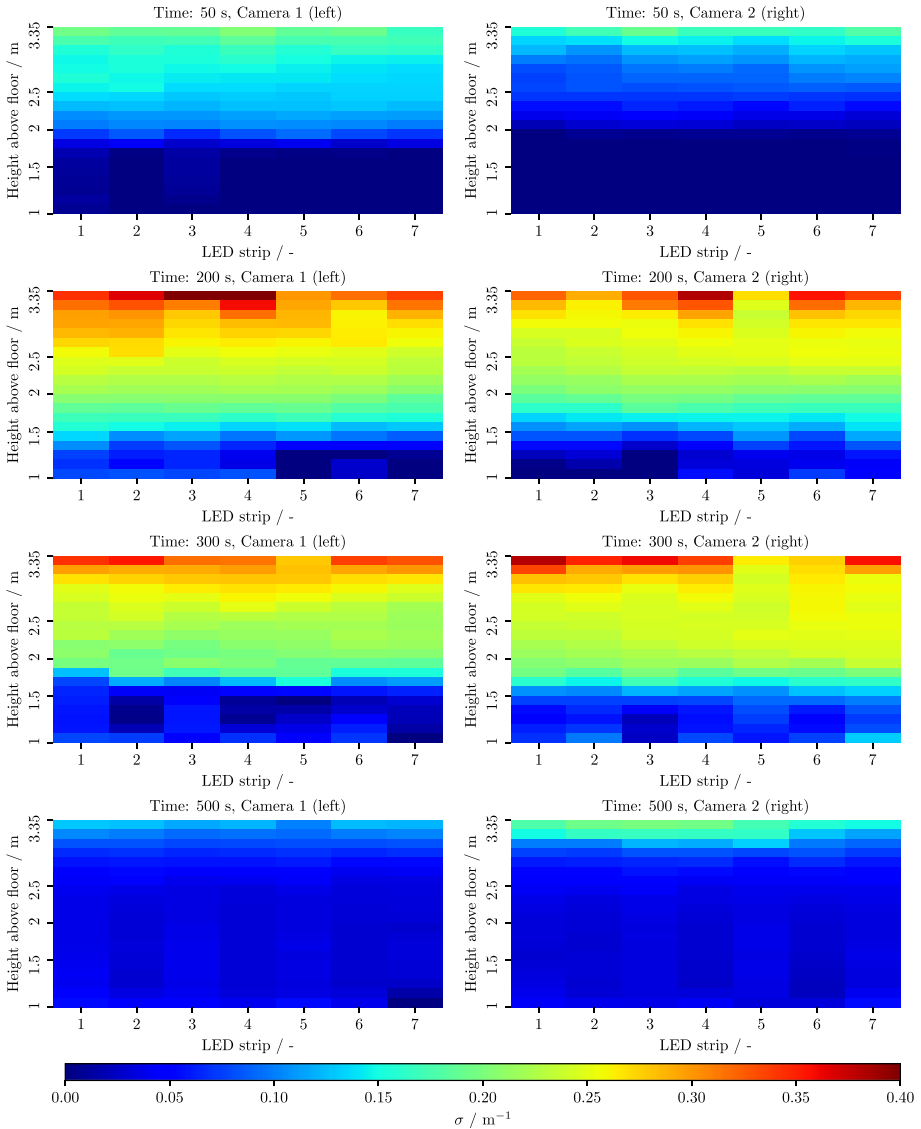


Figure 13. 2D spatial resolution of calculated extinction coefficients for the green camera channel (Channel 1) at different times for both cameras (Color figure online).

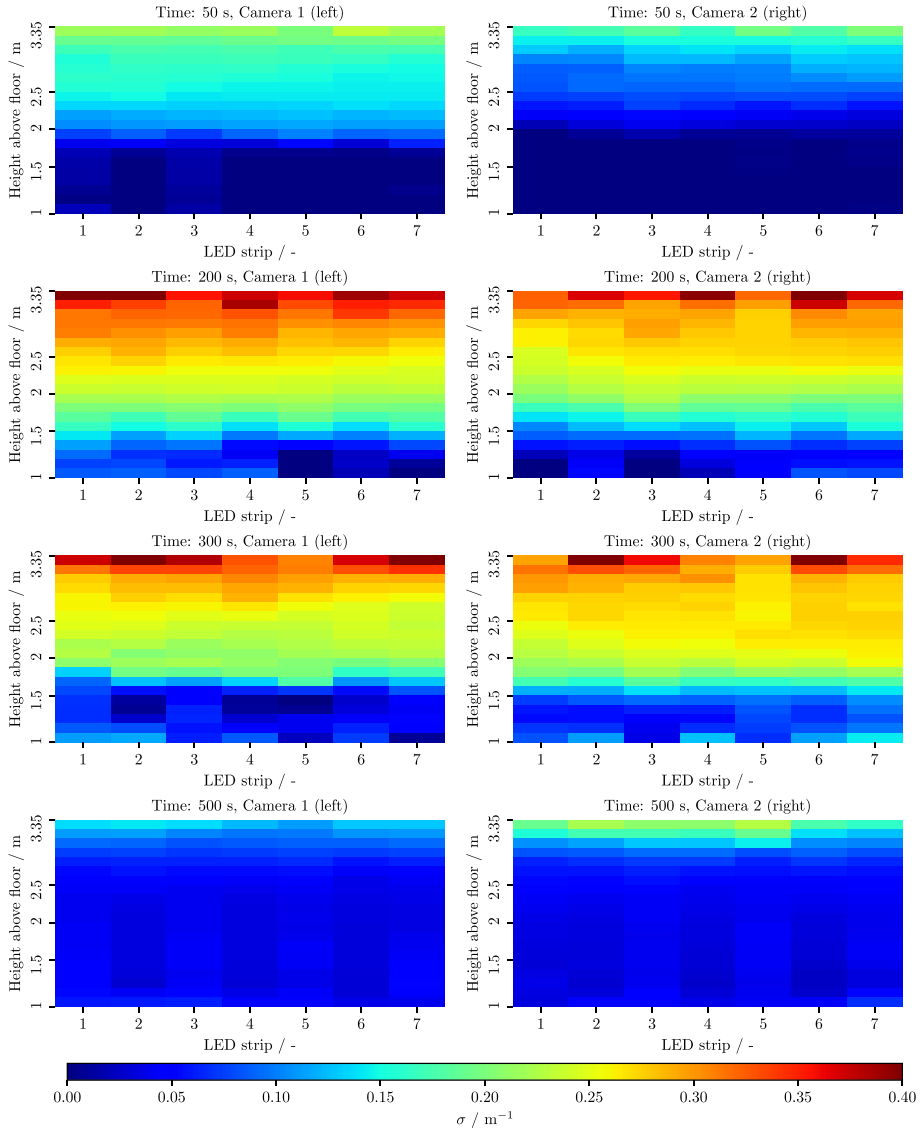


Figure 14. 2D spatial resolution of calculated extinction coefficients for the blue camera channel (Channel 2) at different times for both cameras (Color figure online).

References

1. Purser DA, McAllister JL (2016) Assessment of hazards to occupants from smoke, toxic gases, and heat. In: Hurley MJ (ed) SFPE handbook of fire protection engineering Springer, New York. [10.1007/978-1-4939-2565-0](https://doi.org/10.1007/978-1-4939-2565-0)
2. Cooper LY (1983) A concept for estimating available safe egress time in fires. *Fire Saf J* 5(2):135–144. [https://doi.org/10.1016/0379-7112\(83\)90006-1](https://doi.org/10.1016/0379-7112(83)90006-1)
3. Hartzell GE, Emmons HW (1988) The fractional effective dose model for assessment of toxic hazards in fires. *J Fire Sci* 6(5):356–362. <https://doi.org/10.1177/073490418800600504>
4. Schröder B (2016) Multivariate methods for life safety analysis in case of fire. PhD thesis
5. Schröder B, Arnold L, Seyfried A (2020) A map representation of the ASET-RSET concept. *Fire Saf J* 115:103154. <https://doi.org/10.1016/j.firesaf.2020.103154>
6. McGrattan K, Hostikka S, Floyd J, McDermott R, Vanella M (2022) Fire dynamics simulator user's guide - Version 6.7.9. Technical report
7. Jin T (1970). Visibility through fire smoke (I). *Bull Jpn Assoc Fire Sci Eng* 19(2):1–8. <https://doi.org/10.11196/kasai.19.2.1>
8. Gottuk D, Mealy C, Floyd J (2008) Smoke Transport and FDS Validation. *Fire Saf Sci* 9:129–140. <https://doi.org/10.3801/iafss.fss.9-129>
9. Arnold L, Belt A, Schulze T, Mughal AW (2021) Experimental and numerical investigation of visibility in compartment fires. In: AUBE 21. Universität Duisburg-Essen, Duisburg
10. Arnold L, Belt A, Schultze T, Sichma L (2020) Spatiotemporal measurement of light extinction coefficients in compartment fires. *Fire Mater* . <https://doi.org/10.1002/fam.2841>
11. Ellingham J, Weckman E (2019) Video analysis of smoke density in full-scale fires. In: Combustion institute—Canadian section spring technical meeting 2019. The University of British Columbia, Kelowna
12. Mulholland GW (2002) Smoke production and properties. In: DiNenno PJ (ed) SFPE handbook of fire protection engineering, 3rd edn. National Fire Protection Association, New York
13. Patterson EM, Duckworth RM, Wyman CM, Powell EA, Gooch JW (1991) Measurements of the optical properties of the smoke emissions from plastics, hydrocarbons, and other urban fuels for nuclear winter studies. *Atmos Environ A Gen Top* 25(11):2539–2552. [https://doi.org/10.1016/0960-1686\(91\)90171-3](https://doi.org/10.1016/0960-1686(91)90171-3)
14. Dobbins RA, Jizmagian GS (1966) Particle Size Measurements Based on Use of Mean Scattering Cross Sections. *J Opt Soc Am* 56(10):1351–1354. <https://doi.org/10.1364/josa.56.001351>
15. Mulholland GW, Croarkin C (2000) Specific extinction coefficient of flame generated smoke. *Fire Mater* 24(5):227–230. [https://doi.org/10.1002/1099-1018\(200009/10\)24:5<227::aid-fam742>3.0.co;2-9](https://doi.org/10.1002/1099-1018(200009/10)24:5<227::aid-fam742>3.0.co;2-9)
16. McGrattan K, Hostikka S, Floyd J, McDermott R, Vanella M (2022) Fire dynamics simulator technical reference guide volume 2: Verification—version 6.7.9. Technical report
17. Widmann JF (2003) Evaluation of the planck mean absorption coefficients for radiation transport through smoke. *Combust Sci Technol* 175(12):2299–2308. <https://doi.org/10.1080/714923279>

18. Keller A, Loepfe M, Nebiker P, Pleisch R, Burtscher H (2006) On-line determination of the optical properties of particles produced by test fires. *Fire Saf J* 41(4):266–273. <https://doi.org/10.1016/j.firesaf.2005.10.001>
19. Flecknoe-Brown KW, Hees Pv (2015) Obtaining additional smoke characteristics using multi-wavelength light transmission measurements. In: 14th international conference and exhibition on fire and materials 2015. Interscience communications, San Francisco
20. Cashdollar KL, Lee CK, Singer JM (1979) Three-wavelength light transmission technique to measure smoke particle size and concentration. *Appl Opt* 18(11):1763. <https://doi.org/10.1364/ao.18.001763>
21. Węgrzyński W, Antosiewicz P, Fangrat J (2021) Multi-wavelength densitometer for experimental research on the optical characteristics of smoke layers. *Fire Technol* 57(5):2683–2706. <https://doi.org/10.1007/s10694-021-01139-5>
22. Cerberus (1992) Ionization measuring chamber MIC extinction measuring equipment MIREX. Technical description
23. The European Committee for Standardization (2000) EN 54 Fire detection and fire alarm systems, part 7: smoke detectors point detectors using scattered light, transmitted light or ionization
24. Khan MM, Tewarson A, Chaos M (2016) Characteristics of materials and generation of fire products. In: Hurley MJ (ed) *SFPE handbook of fire protection engineering*. Springer, New York. <https://doi.org/10.1007/978-1-4939-2565-0>
25. Losson O, Macaire L, Yang Y (2010) Comparison of Color Demosaicing Methods. *dv Imaging Electron Phys* 162:173–265. [https://doi.org/10.1016/s1076-5670\(10\)62005-8](https://doi.org/10.1016/s1076-5670(10)62005-8)
26. Tutubalin A (2021) LibRaw. <https://www.libraw.org>
27. Rotjberg P (2017) Processing RAW images in python. Technical report
28. Börger K, Belt A, Arnold L (2023) LEDSA: A python package for determining spatially and temporally resolved extinction coefficients of fire smoke: submitted to JOSS. J Open Source Software
29. Kearney SP, Pierce F (2012) Evidence of soot superaggregates in a turbulent pool fire. *Combust Flame* 159(10):3191–3198. <https://doi.org/10.1016/j.combustflame.2012.04.011>
30. Jin T (1974) Visibility through fire smoke (IV). *Bulletin of Japan Association for Fire Science and Engineering*
31. Mulholland GW (1982) How well are we measuring smoke?. *Fire Mater* 6(2):65–67. <https://doi.org/10.1002/fam.810060205>
32. Gigahertz Optik BTS256-LED Tester (2020) Technical description
33. Schubert EF (2006) *Light-emitting diodes*, 2nd edn. Cambridge University Press, New York. <https://doi.org/10.1017/CBO9780511790546>
34. Börger K, Belt A, Schultze T, Arnold L (2023) Remote sensing of the light-obscuring smoke properties in real-scale fires using a photometric measurement method-data set. <https://doi.org/10.5281/zenodo.7016689>